Journal of Power Sources 677 (2026) 239984

Contents lists available at ScienceDirect

Journal of Power Sources

journal homepage: www.elsevier.com/locate/jpowsour

Enhancements of photoelectrochemical activity and hydrogen evolution of rGO–Ho–TiO_2 nanotubes by rGO optimization

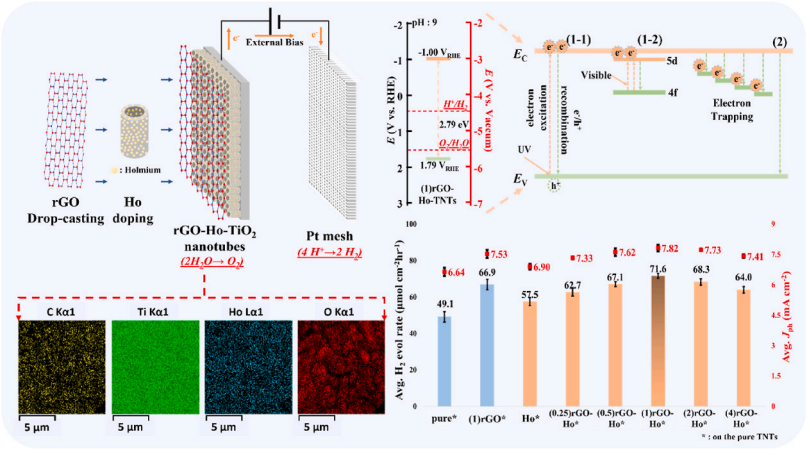
Hyeonmin Jung [a,b], Minseo Kim [a,c], Hyekyung Cho [a,d], Hyunku Joo [a], Kyoung-Soo Kang [a], Hyunjoon Lee [a], Hansung Kim [c], Yeomin Yoon [e], Jaekyung Yoon [a,*], Kwangbok Yi [b,**]

[a] Hydrogen Research Department, Korea Institute of Energy Research, 152 Gajeong-ro, Yuseong-gu, Daejeon 34129, Republic of Korea
[b] Graduate School of Energy Science and Technology Chungnam National University, 99 Daehak-ro, Yuseong-gu, Daejeon 34134, Republic of Korea
[c] Department of Chemical and Biomolecular Engineering, Yonsei University, 50, Yonsei-ro, Seodaenum-gu, Seoul 03722, Republic of Korea
[d] Center of Water Cycle Research, Korea Institute of Science and Technology, 5 Hwarang-ro 14-gil, Seongbuk-gu, Seoul 02792, Republic of Korea
[e] Department of Environmental Science, Ewha Womans University, 52 Ewhayeodae-gil, Seodamun-gu, Seoul 03760, Republic of Korea

HIGHLIGHTS

- Reduced graphene oxide (rGO) drop-cast onto Ho-doped TiO_2 nanotubes (rGO–Ho–TNTs).
- Anode photoelectrochemical performance was optimized by adjusting the rGO content.
- The optimized anodes show improved e^-–h^+ separation and a narrower bandgap.

GRAPHICAL ABSTRACT



ARTICLE INFO

Keywords:
TiO_2 nanotubes
Holmium doping
Reduced graphene oxide
Photoelectrochemical system
Hydrogen production
Band gap engineering

ABSTRACT

Anatase TiO_2 primarily absorbs UV light, but holmium (Ho) doping can achieve visible-light activity. Furthermore, reduced graphene oxide (rGO) can enhance the photoelectrochemical (PEC) properties of photocatalytic electrodes. It is the first systematic study on Ho-doped TiO_2 nanotubes prepared by rGO drop-casting (rGO–Ho–TNTs) with systematically controlled rGO content. The photoelectrochemical properties of the nanotubes for hydrogen evolution via water electrolysis were investigated. The rGO content on the electrode surface significantly affects electrode activity, with 1 μg cm^{-2} identified as the optimal rGO concentration. The corresponding electrode exhibits the highest photocatalytic performance, with a hydrogen evolution rate and photocurrent density enhanced by approximately 1.5 times (71.6 μmol $cm^{-2}h^{-1}$) and 1.2 times (7.82 mA cm^{-2}),

* Corresponding author.
** Corresponding author.
E-mail addresses: jyoon@kier.re.kr (J. Yoon), cosy32@cnu.ac.kr (K. Yi).

https://doi.org/10.1016/j.jpowsour.2026.239984
Received 5 February 2026; Received in revised form 18 March 2026; Accepted 23 March 2026
Available online 26 March 2026
0378-7753/© 2026 The Authors. Published by Elsevier B.V. This is an open access article under the CC BY license (http://creativecommons.org/licenses/by/4.0/).

respectively, compared with those obtained for pure TNTs. Furthermore, we developed a synergistic solar-activated photocatalyst that suppresses the recombination of photogenerated electron–hole (e^-/h^+) pairs, stabilizes the interfacial electronic structure, and promotes charge separation, offering a potential route to high-performance water splitting and sustainable energy applications.

1. Introduction

Titanium dioxide (TiO_2) is widely used in photoelectrochemical (PEC) systems for hydrogen production owing to its, excellent electronic band structure, high photochemical stability, low photocorrosion, and environmental friendliness [1–3]. However, despite these advantages, TiO_2 has a relatively wide bandgap (E_g = 3.2 eV for anatase), which limits its photocatalytic activity due to the rapid recombination of photogenerated electron–hole (e^-/h^+) pairs [1,3,4]. To overcome this limitation, previous studies utilized TiO_2 nanotube (TNT) photoanodes fabricated by anodic oxidation [2,5,6]; however, their ability to utilize light energy remains limited [6–9]. Therefore, to utilize a wider range of solar energy, the absorption wavelength range of photocatalysts must be expanded, and the rapid recombination of photogenerated e^-/h^+ pairs must be suppressed. Various strategies have been proposed to enhance the performance of TiO_2 photocatalysts, including metal doping [2,4,7,8] and the incorporation of carbon allotropes [9,10], which enhance electrode performance by suppressing charge recombination through electron trapping [2,4,7,8,10].

Various doping strategies have been explored to enhance the performance of TiO_2, among which lanthanide metal doping has been reported to be particularly effective [2,4,7,8,11–14]. Among the lanthanides, holmium (Ho) is considered an effective dopant for TiO_2. When Ho ions are incorporated into the TiO_2 lattice, the partially filled 4f orbitals and empty 5d orbitals enable the absorption of a broader range of light wavelengths. This process increases the number of excited electrons, thereby reducing the E_g and energy barrier value of the rate-limiting step, enhancing photoactivity [8,9,11,14]. However, the 4f electrons are shielded by the outer $5s^2$ and $5p^6$ orbitals, which limits their interaction with the host lattice. At excessive dopant concentrations, charge-transfer characteristics can deteriorate due to this shielding effect; therefore, optimizing the doping level is crucial [15,16]. Oxygen vacancies are generated due to the formation of Ti–O–Ho bonds. These oxygen vacancies and Ti^{3+} states are introduced into the conduction band (E_C), improving charge transport through charge hopping and mitigating charge imbalance caused by passivation at the TiO_2 lattice defect sites. As a result, the reaction efficiency increases through the trapping effect of photogenerated e^-/h^+ pairs [11,12]. Furthermore, spin-polarized density functional theory calculations based on the plane-wave pseudopotential method revealed that the formation of surface defects, including oxygen vacancy sites on the surface, sub-surface and titanium vacancy sites on the surface, enhances the stability of Ho–TNTs. The synergistic effect between Ho-f states and surface defects reduces the valance band (Ev) to E_C excitation energy under visible-light irradiation, facilitating photoexcitation and thereby enhancing visible light-driven photocatalytic activity [17].

Recent research trends indicate that carbon allotropes have been widely investigated for photothermal conversion [18–21] and photocatalytic reactions [13,22–24]. Among them, in photocatalytic research, graphene has been shown to significantly enhance PEC electrode performance owing to its high electrical conductivity and large surface area [12]. In particular, graphene oxide (GO) is relatively easy and economical to synthesize. However, excessive oxygen-containing functional groups (carboxyl, hydroxyl, carbonyl, and epoxide) are generated during the oxidation process, leading to numerous structural defects in the GO lattice that reduce electrical conductivity. However, converting GO into reduced graphene oxide (rGO) through methods such as annealing or hydrothermal treatment can enhance the PEC properties, suppress the recombination rate of e^-/h^+ pairs, and increase the photoreactive surface area, thereby improving the overall electrode performance [13,22–26]. Furthermore, density functional theory simulations indicate that oxygen-containing functional groups on rGO (epoxy or hydroxyl) interact with Ti to form Ti–O–C bonds, while the plane-averaged charge-density difference upon electron transfer provides evidence for electron migration from rGO to TiO_2 [27,28]. The resulting interfacial charge redistribution promotes the accumulation of electron polarization at the rGO–TiO_2 interface and increases the density of active sites for photochemical reactions. Therefore, composites containing rGO, which exhibits interfacial charge transfer and redistribution, is considered an effective electrode material for photoelectrochemical applications [27]. However, in the case of TiO_2 modified solely with rGO, sustained efficiency during long-term operation may be limited due to an increase in internal resistance [29].

Wang et al. [26] fabricated rGO–TNT photoanodes using an anodic oxidation method combined with cyclic voltammetry. The photocurrent density and photoconversion efficiency of an rGO–TNT electrode were approximately 1.3 times (from 5.62 to 7.49 mA cm^{-2}) and 1.4 times (from 3.14 to 4.48%) higher, respectively, than those of pure TNTs. Similarly, Cho et al. [9] doped TNTs with erbium (Er) and drop-cast rGO to fabricate rGO–Er–TNT electrodes. Compared to pure TNTs, the hydrogen evolution rate increased by approximately 10.8 times (from 10.65 to 115.37 μmol $cm^{-2}h^{-1}$) PCE increased by approximately 7.2 times (from 0.32 to 2.3%) and the E_g decreased by approximately 0.9 times (from 2.80 to 2.52 eV). Girisun et al. [30] fabricated Au/rGO@-TiO_2 nanorod photoanode DSSC and the efficiency was increased by about 1.8 times (from 3.73 to 6.74%). Kavitha et al. [31] fabricated rGO@g-C_3N_4/$BiVO_4$ composite and the efficiency was increased by about 1.7 times (from 0.27 to 0.45 %). Yan et al. [32] fabricated a Si/rGO/MoS_2 composite, achieving a maximum efficiency of 3.4%. Previous studies have demonstrated that rGO incorporation increases the photogenerated carrier density and open-circuit potential, enhances efficiency by suppressing e^-/h^+ recombination and improving charge separation, and reduces the E_g by extending the photoactive and absorption wavelength range [9,13,22–26].

Although several recent studies have investigated the synthesis of rGO–noble metal–TNT composites, research on rGO–Ho–TNT composites has not yet been reported, despite evidence that Ho exhibits the best PEC photoanode performance among various lanthanide metals [8,9,26]. Therefore, in this study, rGO–Ho–TNTs were synthesized to enhance the light absorption and charge transfer characteristics of photoanodes, and their catalytic activities were evaluated through PEC analysis and water-splitting experiments. Moreover, to comprehensively overcome the limitations of previous studies, the Ho concentration was fixed to avoid performance degradation arising from the shielding effect at excessive doping levels [15,16], while the excellent electrical conductivity of rGO was exploited to reduce the interfacial charge-transfer resistance and promote electron transport [29].

2. Materials and methods

2.1. Preparation of pure TNTs and Ho-TNTs

Pure TNTs were prepared by anodization and electrochemical doping processes. Ti foil (0.3 mm thick, 99.7%, Goodfellow, England) was cut into pieces with dimensions of 2.5 × 5 cm, and surface impurities were removed using an ultrasonic cleaner with deionized (DI) water and ethanol (C_2H_6O, Duksan Chemicals Co., Korea) for 30 min each. The cleaned Ti foil was then etched with diluted hydrofluoric acid

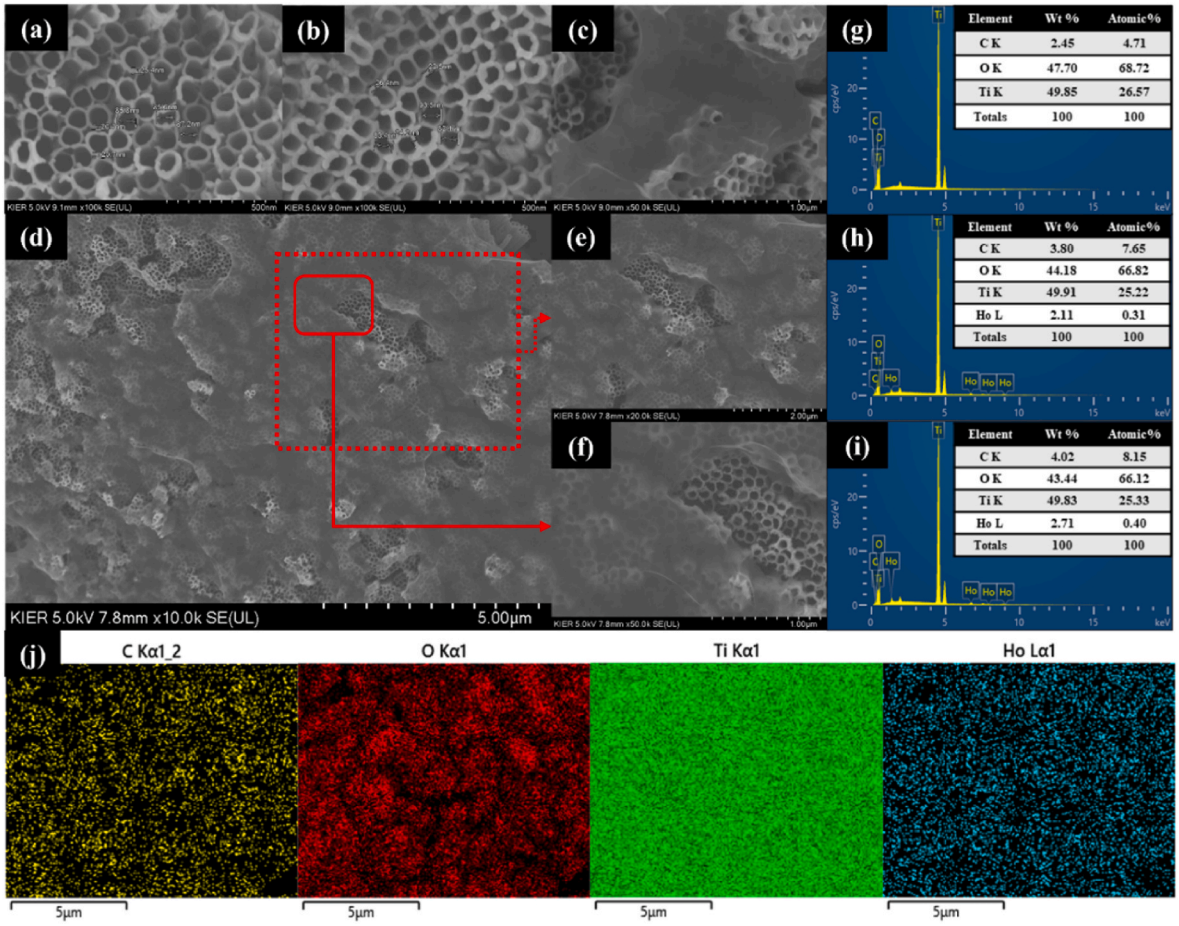


Fig. 1. SEM images of (a) (a) pure TNTs, (b) Ho-TNTs, (c) GO–Ho–TNTs, and (d-f) rGO–Ho–TNTs; EDS spectra of (g) pure TNTs, (h) GO–Ho–TNTs, and (i) rGO–Ho–TNTs; (j) scanning transmission electron microscopy elemental maps for rGO–Ho–TNTs. Here, the amount of GO and rGO on the electrode surface is 1 μg cm^{-2}.

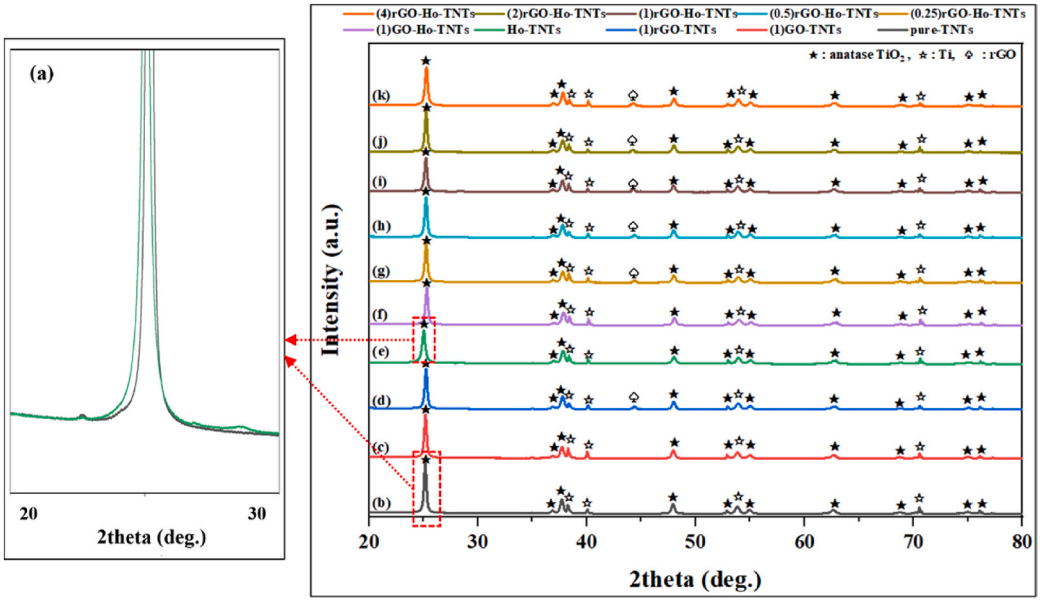


Fig. 2. (A) Magnified XRD view of the (101) peak for pure TNTs and Ho–TNTs, (B) XRD patterns of the as-prepared samples. Here, (x) represents the amount of rGO (μg cm^{-2}).

(HF; 48.5–52.0%, Duksan Chemicals Co., Korea), rinsed thoroughly with DI water, and dried at room temperature (~25 °C) for 24 h [33]. During anodization, Ti foil was used as the anode, and Fe foil (0.25 mm thick, 2.5 × 6 cm) as the cathode. The electrolyte consisted of a mixture of 0.5

Table 1
Structural properties of the as-prepared samples. Here, (x) represents the amount of rGO (μg cm^{-2}).

	Samples	Cell parameter (Å)			Cell volume V (Å^3)	Crystallite size (Å)
		a, Å	b, Å	c, Å		
1	**Pure TNTs**	3.78	3.78	9.49	135.26	338
2	**Ho-TNTs**	3.79	3.79	9.51	136.28	314
3	**(1)GO-TNTs**	3.78	3.78	9.51	136.23	351
4	**(1)GO-Ho-TNTs**	3.79	3.79	9.51	136.30	323
5	**(1)rGO-TNTs**	3.78	3.78	9.51	136.21	280
6	**(0.25)rGO-Ho-TNTs**	3.79	3.79	9.50	136.25	286
7	**(0.5)rGO-Ho-TNTs**	3.78	3.78	9.51	136.21	278
8	**(1)rGO-Ho-TNTs**	3.78	3.78	9.47	135.28	261
9	**(2)rGO-Ho-TNTs**	3.79	3.79	9.49	136.15	269
10	**(4)rGO-Ho-TNTs**	3.78	3.78	9.51	136.23	284

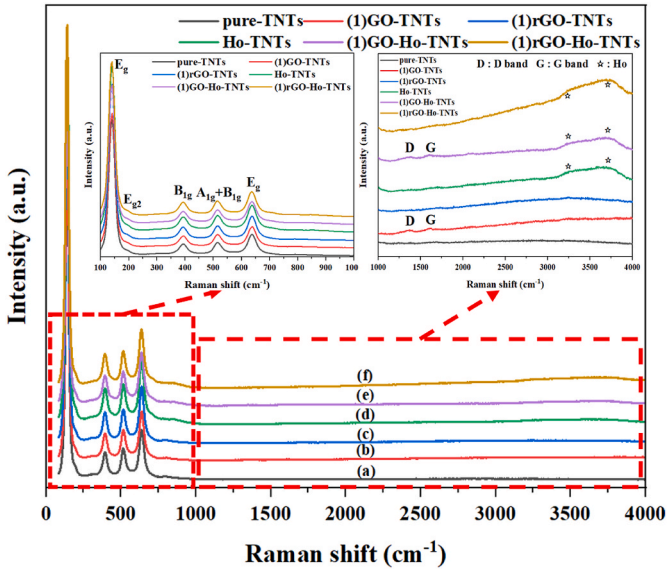


Fig. 3. Raman spectra of the as-prepared samples: (a) pure TNTs, (b) (1) GO–TNTs, (c) (1)rGO–TNTs, (d) Ho–TNTs, (e) (1)GO–Ho–TNTs, and (f) (1)rGO–Ho–TNTs.

M ammonium fluoride (NH_4F; >97%, Junsei Chemical Co., Japan), 2 vol % DI water, and ethylene glycol ($C_2H_6O_2$; >99.5%, Duksan Chemicals Co., Korea). Anodization was performed in a two-electrode configuration under a constant current of 0.1 A for 150 min. The as-prepared amorphous TNTs were washed several times with DI water and dried at ~25 °C for 2 d. Subsequently, the pure TNTs electrodes were obtained by annealing at 450 °C for 2 h in an oxygen atmosphere (400 mL min^{-1}). Ho–TNTs were fabricated using a previously prepared amorphous TNT electrode as the anode (working electrode), a Pt mesh (52 mesh, 5 × 5 cm, 99.9%, trace metals basis, Sigma-Aldrich, USA) as the cathode (counter electrode), and a precursor solution containing holmium (III) nitrate pentahydrate ($Ho(NO_3)_3{\cdot}5H_2O$, 99.9%, Sigma-Aldrich, USA) as the precursor solution. Electrochemical doping was performed for 100 s at a current density of −1.0 mA cm^{-2} using a 0.01 wt% Ho precursor solution adjusted to pH 7 with 0.01 M sodium hydroxide solution (NaOH; Samchun Chemicals Co., Korea) [7]. The doped electrode was then rinsed with DI water, dried in a desiccator for 2 d, and subjected to heat treatment under the same conditions as the pure TNT electrode.

2.2. Preparation of rGO electrodes

To prepare GO–TNTs, GO–Ho–TNTs, rGO–TNTs, and rGO–Ho–TNTs, 50 μL of 0.00125 wt% GO dispersion was drop-cast onto the surfaces of pure TNTs and Ho–TNTs. The actual amount of rGO was calculated from the concentration of the dispersion, in which one 50 μL drop corresponded to 0.625 μg of GO. The dispersion solution was then drop-cast onto the electrode surface in 0, 4, 8, 16, 32, and 64 drops to obtain rGO content of 0, 0.25, 0.5, 1, 2, and 4 μg on a 10 cm^2 electrode, respectively. After drop-casting, the electrodes were dried for 2 d to obtain GO–TNTs and GO–Ho–TNTs, followed by annealing at 450 °C for 2 h in an Ar atmosphere (400 mL min^{-1}) to reduce GO to rGO.

2.3. Characterization experiments

Field-emission scanning electron microscopy (FE-SEM; Regulus 8220; Hitachi, Japan) and energy-dispersive X-ray spectroscopy (EDS; 65 mm^2 SDD, ULTIM MAX, Oxford, UK) were employed to examine the surface morphology and elemental composition of the electrodes, respectively. The crystalline phases of the samples were identified using high-resolution X-ray diffraction (XRD; SmartLab, Rigaku, Japan) with Cu Kα radiation (λ = 0.15418 nm, 45 kV and 200 mA) over a 2θ range of 20°–80°. High-resolution Raman spectroscopy (LabRAM HR Evolution Visible-NIR, Horiba, Japan) was utilized to confirm the presence of GO and rGO and to investigate the chemical bonding states. The catalysts were measured over the wavenumber range of 100–3500 cm^{-1} using a 514 nm excitation laser source.

To more precisely determine the chemical bonding states between materials, X-ray photoelectron spectroscopy (XPS; NEXSA G2, Thermo Fisher Scientific, USA) was performed using a monochromatic Al Kα X-ray source. The optical absorption characteristics and E_g of the photocatalysts were analyzed over the wavelength range of 300–1000 nm using ultraviolet–visible diffuse reflectance spectroscopy (UV-DRS; SolidSpec-3700, Shimadzu, Japan). Additionally, ultraviolet photoelectron spectroscopy (UPS; NEXSA G2, Thermo Fisher Scientific, USA) was used to calculate the E_V and E_C positions based on the work function (Φ), low binding energy (E_L), and Fermi level (E_F) values obtained from band-structure analysis.

2.4. Electrochemical analysis

Electrochemical properties were analyzed using an electrochemical analyzer (ZIVE, WonATech, Korea) in a three-electrode system. The fabricated photoanode was cut to an appropriate size and mounted on a Teflon holder with an exposed photoactive area of 1 cm^2 serving as the working electrode. A platinum wire (2.6 g, diameter = 1.0 mm, 99.9% trace metals basis; Sigma-Aldrich, USA) and a Hg/HgO electrode (1.0 M NaOH internal solution) were employed as the counter and reference electrodes, respectively. A 0.1 M Na_2SO_3 aqueous solution was used as the electrolyte. SO_3^{2-} has a lower oxidation potential than water and acts as a hole scavenger by consuming photogenerated holes, thereby suppressing charge recombination and promoting charge separation [34–36]. The illumination source was a 1000 W xenon lamp (Newport, USA) equipped with a 10 cm infrared water filter. The light intensity was calibrated to 44,000 μW cm^{-2} using a portable radiometer (UM320, Minolta Co., Japan). Electrochemical measurements were sequentially conducted in the following order: open-circuit potential (OCP), linear sweep voltammetry (LSV), chronoamperometry (CA), photo-conversion efficiency (PCE) and electrochemical impedance spectroscopy (EIS).

2.5. Photoelectrochemical water splitting system

The hydrogen evolution rate was measured using a PEC cell using a two-electrode system under various conditions. A platinum mesh (1 cm^2) was employed as the counter electrode, while the working electrode, electrolyte, and illumination conditions were identical to those

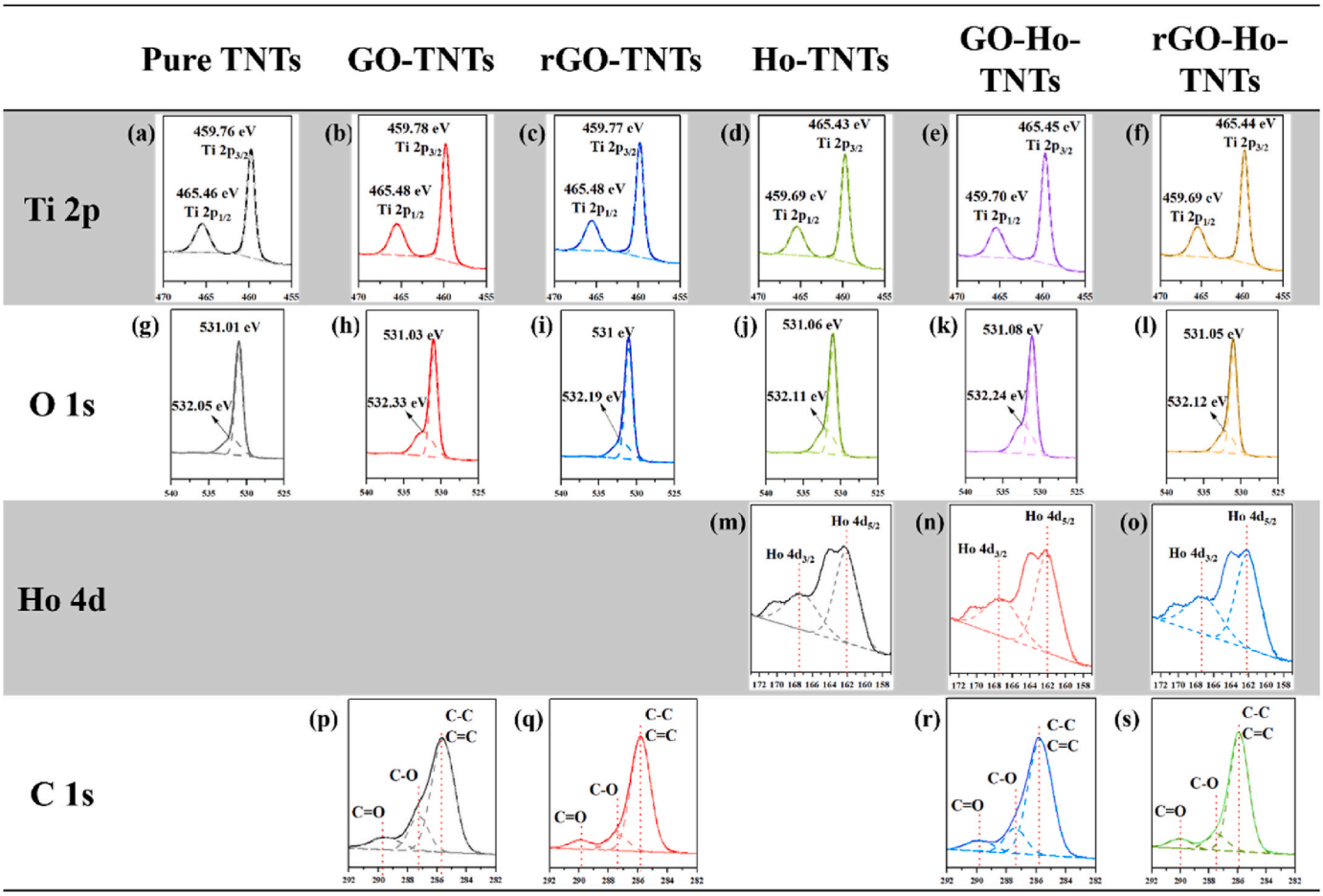


Fig. 4. XPS spectra of the as-prepared samples: (a-f) Ti 2p, (g-l) O 1s, (m-o) Ho 4p, and (p-s) C 1s spectra. Here, the amount of GO and rGO on the electrode surface is 1 μg cm^{-2}.

used in the electrochemical measurements. Before each experiment, the reactor was purged with Ar for 30 min to remove residual O_2, N_2, and other gases that might be present in the system. Subsequently, the potential difference between the two electrodes was set to 1.5 V using an interactive digital source meter (2450 Source meter, Keithley, USA). The H_2 generated during the water-splitting experiment was quantitatively analyzed using gas chromatography (GC; 7890A; Agilent Technologies, USA).

3. Results and discussion

3.1. Surface and structural properties

Fig. 1 shows the surface morphology and elemental composition of pure TNTs, Ho–TNTs, GO–Ho–TNTs, and rGO–Ho–TNTs obtained by SEM and EDS analyses, respectively. As shown in Fig. 1(b), electrochemical Ho-doping does not affect the basic structure of the TNTs, which is characterized by an array of uniform vertical cylindrical structures, with pore diameters of 82.4–93.5 nm, wall thicknesses of 22.5–26.4 nm, and open tops. No impurities were identified in any of the samples in Fig. 1(a and b). Fig. 1(c–f) confirm that thin films of GO and rGO cover the TNT surfaces.

The EDS results in Fig. 1(g–i) show that the C content of the GO–Ho–TNTs is 1.35 wt% higher than that of the Ho–TNTs, confirming the formation of a GO layer. Compared to GO–Ho–TNTs, rGO–Ho–TNTs show a 0.22 wt% higher C content and 0.74 wt% lower O content, indicating that rGO was formed during the reduction process. Finally, Fig. 1(j) confirms that the Ti, O, C, and Ho elements are uniformly distributed.

The XRD patterns in Fig. 2 were obtained to investigate the variations in crystal phase and crystallite size between the samples. The XRD patterns for all samples exhibit the characteristic diffraction peaks of anatase TiO_2, corresponding to the (101), (103), (004), (200), (105), (211), (204), (116), (215), and (301) planes at 2θ = 25.21°, 36.84°, 37.71°, 47.84°, 52.93°, 54.94°, 62.47°, 68.57°, 74.98°, and 76.11°, respectively (JCPDS No. 00-021-1272). Ho doping and rGO bonding did not induce any phase transition, indicating that the anatase TiO_2 structure was well maintained for all samples.

Comparing Fig. 2(a), no distinct Ho-related diffraction peaks are observed in the XRD pattern of the Ho-containing samples. However, several peaks appear broadened and slightly shifted toward lower angles after Ho addition. This is attributed to two main factors. First, Ho ions are highly dispersed and present in very small amounts, making their diffraction signals difficult to detect by XRD [37,38]. Second, the ionic radius of the dopant Ho^{3+} (0.901 Å) [39] is larger than that of Ti^{4+} (0.605 Å) [39], which induces lattice tensile strain when Ho atoms substitute at Ti sites in the TiO_2 lattice [37,38]. Therefore, the lattice parameters were found to vary with Ho doping, but structural stability was maintained without affecting the crystal phase of TNTs [37,38]. A summary of the lattice parameters is provided in Table 1.

As shown in Fig. 2(c–f), characteristic diffraction peaks of GO are not observed for GO-containing samples, as the GO content was too low to be detected within the sensitivity limit of XRD [40]. As shown in Fig. 2 (d–g–k), the diffraction peak corresponding to the (002) plane of rGO at 24.6° [26,41] is not clearly observed for the rGO-containing samples, likely because of the low rGO content and any small peaks being

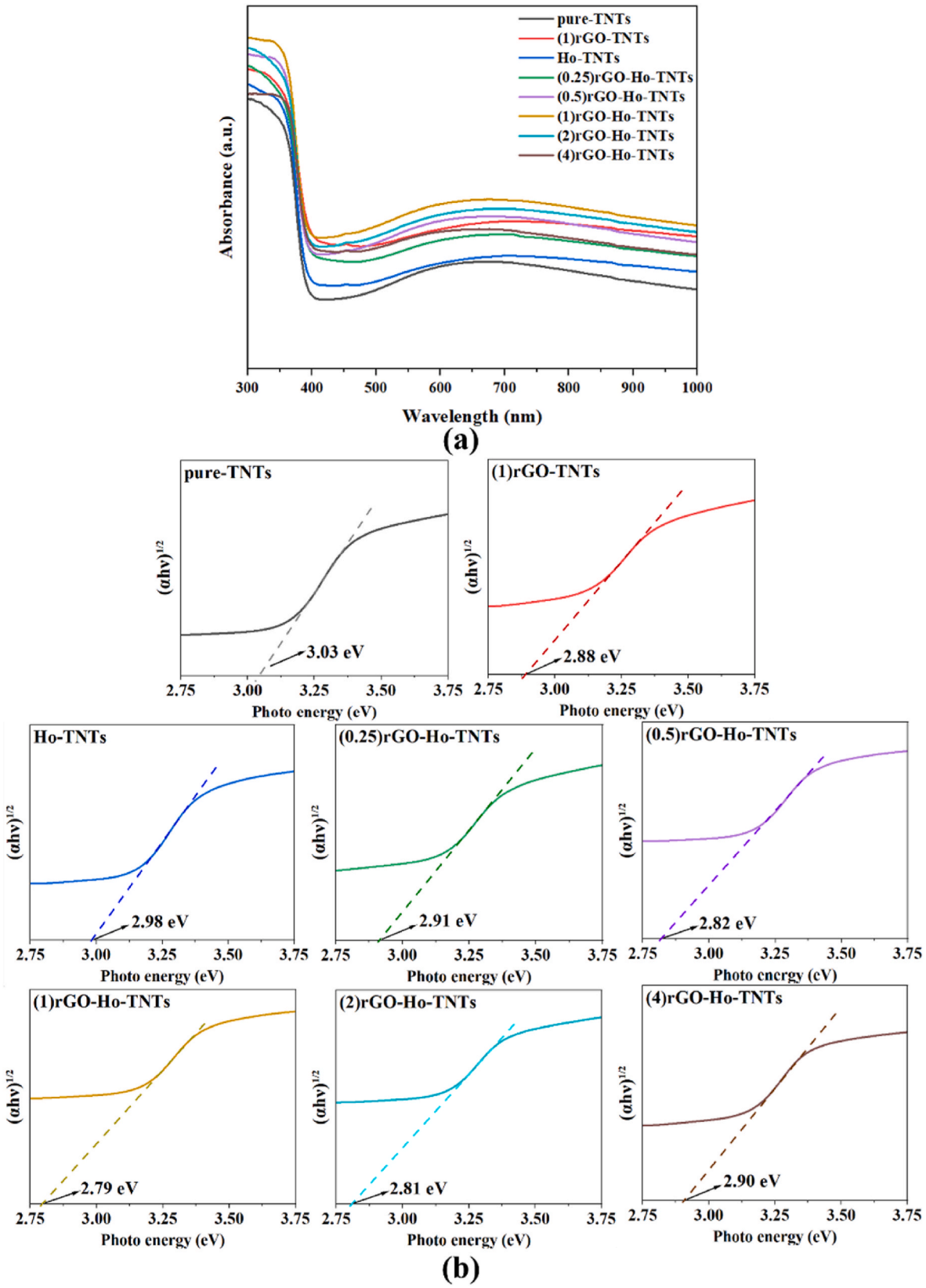


Fig. 5. (a) UV–DRS spectra and (b) Tauc plots of the as-prepared samples. Here, (x) represents the amount of rGO (μg cm^{-2}).

obscured by the intense anatase TiO_2 (101) diffraction peak [41,42]. Additionally, TiO_2 nanoparticles may have been intercalated between GO layers during sample preparation, leading to a partial collapse of the typical graphene stacking structure [43]. Instead, the presence of rGO (101) was confirmed by diffraction peaks observed around 2θ = 44.3°–44.4° (Fig. 2(d–g–k)). The crystallite sizes, calculated using the Scherrer equation [40,42], are summarized in Table 1. After Ho doping and rGO drop-casting, a smaller crystallite size is observed compared to

Table 2
Band structure parameters of the as-prepared samples relative to the vacuum level. Here, (x) represents the amount of rGO (μg cm^{-2}).

	Samples	Low binding energy (E_L, eV)	Work function (ϕ, eV)	Valence band (E_V, eV)	Band gap (E_g, eV)	Conduction band (E_C, eV)
1	**Pure TNTs**	2.94	3.72	−6.66	3.03	−3.63
2	**(1)rGO-TNTs**	2.61	3.42	−6.03	2.88	−3.15
3	**Ho-TNTs**	2.87	3.63	−6.5	2.98	−3.52
4	**(0.25) rGO-Ho-TNTs**	2.69	3.53	−6.22	2.91	−3.31
5	**(0.5) rGO-Ho-TNTs**	2.59	3.38	−5.97	2.82	−3.15
6	**(1)rGO-Ho-TNTs**	2.50	3.25	−5.68	2.79	−2.89
7	**(2)rGO-Ho-TNTs**	2.54	3.33	−5.87	2.81	−2.81
8	**(4)rGO-Ho-TNTs**	2.66	3.49	−6.15	2.90	−2.9

pure TNTs, which is attributed to the delayed crystal growth caused by Ho doping [44], the formation of oxygen vacancies, and a decrease in crystallite size [45]. A smaller crystallite size is expected to increase the hydrogen evolution rate by increasing the photoactive surface area. In contrast, the GO-containing samples, (1)GO–TNTs and (1)GO–Ho–TNTs, exhibit larger crystallite sizes, which are expected to exhibit reduced photoactivity because of the lower photoreactive surface area. Therefore, these samples were not investigated further.

Raman spectroscopy was performed to characterize the chemical and structural properties of the samples, and the results are shown in Fig. 3. All TiO_2-based samples exhibit the characteristic vibrational mode peaks of anatase TiO_2 at 141.1 cm^{-1} (E_g), 198.5 cm^{-1} (E_{g2}), 392.8 cm^{-1} (B_{1g}), 515.7 cm^{-1} ($A_{1g} + B_{1g}$), and 636.6 cm^{-1} [46,47]. Fig. 3(d–f) present the Raman spectra for Ho–TNTs, (1)GO–Ho–TNTs, and (1)rGO–Ho–TNTs, in which additional peaks are observed around 3242 and 3703 cm^{-1}. These were confirmed to be characteristic peaks corresponding to Ho^{3+}, not peaks originating from the TiO_2 anatase phase [48].

Fig. 3(b, e) show the Raman spectra of (1)GO–TNTs and (1) GO–Ho–TNTs, respectively. The spectrum for (1)GO–TNTs shows, peaks at 1355.4 cm^{-1} (D band) and 1612.2 cm^{-1} (G band), while the spectrum for (1)GO–Ho–TNTs shows peaks at 1366.1 cm^{-1} (D band) and 1605.2 cm^{-1} (G band), confirming the presence of GO on the TiO_2 surface. The D band is an out-of-plane vibration caused by structural disorder and defects (such as sp^3 components) in the carbon lattice, and is related to the breathing mode of the A_{1g} symmetry k-point phonon. In contrast, the G band provides information about the in-plane E_{2g} vibration of aligned carbon atoms with sp^2 bonds in the first scattering mode [46,49]. The relative intensity ratio of the D and G band peaks (I_D/I_G) is used as an indicator of the degree of carbon crystallinity and structural disorder. In general, a larger I_D/I_G indicates a higher degree of defects and disorder, generally corresponding to higher electronic conductivity, whereas a smaller I_D/I_G indicates a lower defect density and a higher level of carbon graphitization [41,46,49]. An I_D/I_G ratio of 0.995 was calculated for (1)GO–Ho–TNTs. In contrast, as shown in Fig. 3(c–f), the characteristic D and G band peaks are not observed for either (1)rGO–TNTs or (1) rGO–Ho–TNTs. In general, a decrease in I_D/I_G is accompanied by peak broadening and reduced overall intensity, suggesting the reduction of GO, a decrease in defect concentration, and the removal of oxygen-containing functional groups [46,50,51]. Therefore, these results confirm that GO was successfully reduced to rGO via annealing.

XPS was performed to investigate the chemical bonding and chemical state variations based on the Ti 2p, O 1s, C 1s, and Ho 4d spectra for each sample, as shown in Fig. 4. The Ti 2p spectrum for pure TNTs (Fig. 4 (a)) exhibits two peaks at 465.46 eV (Ti $2p_{1/2}$) and 459.76 eV (Ti $2p_{3/2}$), corresponding to Ti^{4+}, which is consistent with the anatase phase [26, 44]. For Ho–TNTs (Fig. 4(d)), a red shift in the Ti binding energy is observed compared with that of pure TNTs, indicating electron accumulation on Ti atoms and the formation of Ti^{3+} species, both of which contribute to enhanced photocatalytic activity [9,26,44]. Furthermore, the weak peak at 459.69 eV in the Ti 2p spectrum for (1)rGO–Ho–TNTs (Fig. 4(f)) indicates the formation of Ti–O–C bonds between rGO and TiO_2 [52,53]. This indicates that interfacial charge redistribution at the electrode interface mediated by Ti–O–C bonding promotes the accumulation of electron polarization, thereby increasing the density of active sites for photochemical reactions [27,28].

The O 1s spectrum for pure TNTs (Fig. 4(g)) shows main peaks at 531.01 and 532.05 eV, assigned to the lattice oxygen of TiO_2 and the surface hydroxyl groups (–OH) of TiO_2, respectively, confirming the formation of Ti–O and Ti–OH species [26,54]. In the case of (1) rGO–Ho–TNTs (Fig. 4(l)), the binding energies are blue-shifted to 531.05 and 532.12 eV compared to those for pure TNTs due to Ho doping and rGO drop-casting. This shift is likely caused by the formation of Ti^{3+} species, an increase in the number of TiO_2 surface oxygen vacancies, and enhanced electronic interactions within the TiO_2 lattice [52,54,55].

The Ho 4d spectra (Fig. 4(m–o)) show spin–orbit components of $4d_{5/2}$ and $4d_{3/2}$ at 162.2 and 167.4 eV, respectively, similar to those of Ho_2O_3, confirming the Ho^{3+}oxidation state [54,56]. In addition, the binding energy of the pure Ho 4d peak shifts from 161.8 to 162.2 eV due to the influence of Ho–O or Ho–O–C chemical bonding [54,57]. XPS results verified the presence of Ho 4f-related bonding on the TNT surfaces. The synergy between Ho-f states and surface defects promotes photoexcitation under illumination by improving charge-carrier processes, which consequently enhances the photocatalytic activity [17, 54].

In the C 1s spectra (Fig. 4(p–s)), three main bonding peaks are identified: C=C/C–C bonds (285.56–285.91 eV, related to sp^2 and sp^3 hybridization), C–O bonds (287.23–287.50 eV, related to epoxy and hydroxyl groups), and C=O bonds (289.5–290.5 eV, related to carbonyl and carboxylic groups) [43,57–59]. For the samples containing GO (Fig. 4(p–r)), the C–O and C=O peak area fractions are 56.8% and 50.8%, respectively, whereas for the samples containing rGO (Fig. 4 (q–s)), these values decrease to 42.8% and 34.7%. This is attributed to the effective cleavage of C–O and C=O bonds during annealing, which reduces the proportion of oxygen-containing functional groups, indicating deoxygenation, i.e., the reduction of GO to rGO [43,57–59]. Therefore, based on the XPS Ti 2p, O 1s, Ho 4d, and C 1s binding energies for rGO–Ho–TNTs, it was confirmed that rGO, GO, and Ho are all successfully bound to the TNTs.

According to the UV-DRS analysis results (Fig. 5(a)), all samples exhibit the typical UV absorption characteristics of anatase TiO_2, with maximum absorption observed in the UV region (<400 nm) corresponding to the electronic transition from O 2p (E_V) to Ti 3d (E_C) [13,25, 26]. In the Ho-doped samples, the light absorption range extends into the visible region, which is attributed to charge transfer between the 4f electron level of Ho^{3+} and the E_C or E_V of TiO_2 [7,14,60,61]. Furthermore, the absorption spectra of the rGO-containing samples exhibit a noticeable red shift and enhanced absorbance in the UV region compared to pure TNTs. Upon light irradiation, the separation efficiency of the photogenerated e^-/h^+ pairs improves, thereby enhancing light absorption and photocatalytic activity [24,25]. The oxygen content in rGO also affects the E_g, which tends to narrow as the oxygen content decreases [53,58]. Among the samples, (1)rGO–Ho–TNTs exhibits the highest absorbance in the visible region, effectively generating e^-/h^+ pairs upon illumination and demonstrating the highest overall efficiency among the studied materials. Since TiO_2-based materials are indirect bandgap semiconductors, the optical E_g (eV) was estimated from the Tauc plot (Fig. 5(b)) by extrapolating the linear portion of the $(\alpha h\nu)^{1/2}$ versus $h\nu$ curve using Equation (1) [26,62].

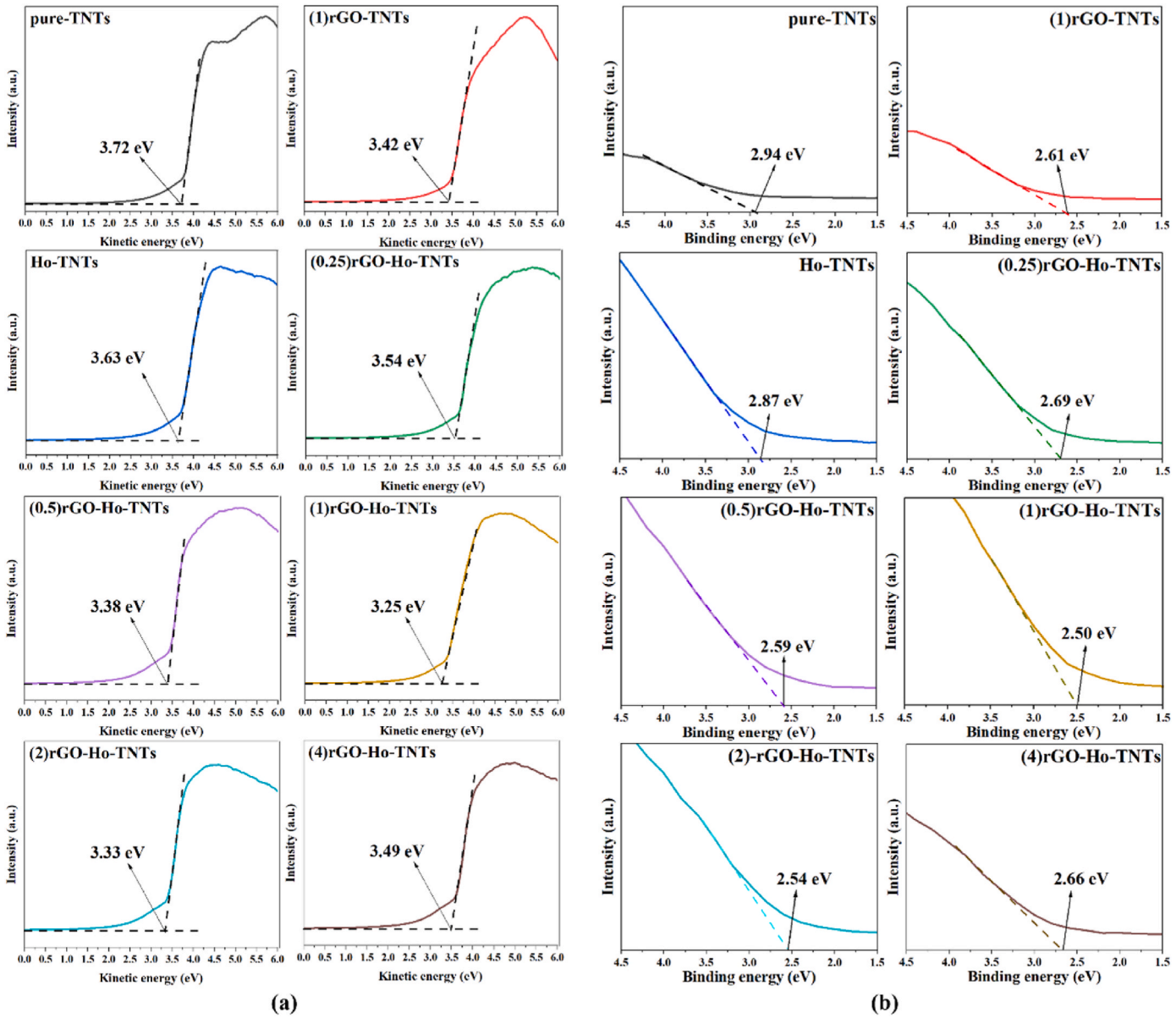


Fig. 6. (a) Work functions and (b) low binding energy plots for the as-prepared samples.

$$(\alpha h\nu)^{1/2} = A(h\nu - E_g) \quad (1)$$

Here, α is the absorption coefficient, h is Planck's constant (6.626×10^{-34} J s), ν is the frequency of light (s^{-1}), and A is a proportionality constant.

The calculated results are summarized in Table 2, showing that the E_g values for the Ho- and rGO-containing samples are lower than that of pure TNTs. In particular, (1)rGO–Ho–TNTs exhibits the lowest E_g of 2.79 eV, which is approximately 0.24 eV lower than that of pure TNTs, corresponding to a shift in the absorption wavelength from ~410 to ~445 nm. This lower E_g is attributed to two main factors. First, the introduction of new energy levels through doping expands E_C, thereby broadening the energy range available for electron movement and enhancing electron excitation efficiency [55]. Second, according to the quantum size effect, in which the semiconductor crystallite size influences the photophysical and spectroscopic properties of the material, a decrease in crystallite size leads to stronger exciton confinement and a more pronounced shift of the absorption edge [9,14]. This observation is consistent with the XRD results, which confirm that the crystallite size of (1)rGO–Ho–TNTs is 22.87% lower than that of pure TNTs.

UPS was conducted to determine the Φ of electrodes fabricated with Ho, rGO, and TNTs. The Φ represents the energy difference between the E_F and the vacuum level (E_{Vac}) and is defined as the minimum energy required to remove an electron from a material's surface. In general, a lower Φ facilitates electron transport, thereby increasing electron transfer efficiency [63]. The Φ values were calculated using Equation (2) and are presented in Fig. 6(a).

$$\Phi = h\nu - (E_{cut-off} - E_F) \quad (2)$$

Here, $h\nu$ is the excitation energy (21.2 eV), and $E_{cut\text{-}off}$ (eV) is the secondary cut-off energy. Based on secondary electron emission, the Φ of pure TNTs was determined to be 3.72 eV. The Φ values of the other samples are as follows: (1)rGO–TNTs (3.42 eV), Ho–TNTs (3.63 eV), (0.25)rGO–Ho–TNTs (3.53 eV), (0.5)rGO–Ho–TNTs (3.38 eV), (1)rGO–Ho–TNTs (3.25 eV), (2)rGO–Ho–TNTs (3.33 eV), and (4)rGO–Ho–TNTs (3.49 eV). Among them, (1)rGO–Ho–TNTs exhibits the lowest Φ (Fig. 6(a)–Table 2). Overall, the Φ values of all Ho-doped and rGO-drop-cast samples are lower than that of the pure TNTs. This is

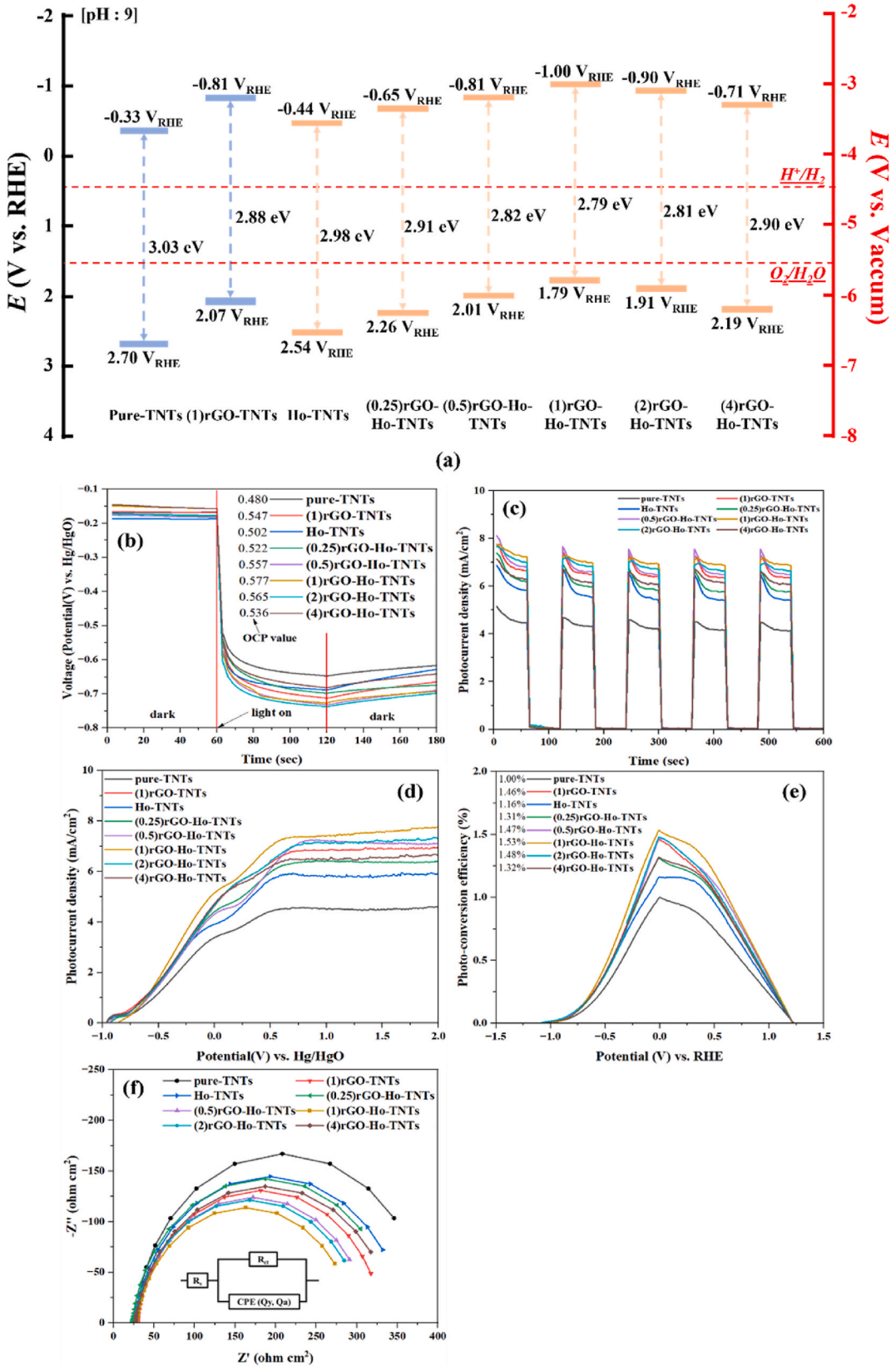


Fig. 7. (a) Band structures of the as-prepared samples in terms of the reversible hydrogen electrode (RHE) and vacuum level. (b-f) Photoelectrochemical analysis of the as-prepared samples: (b) OCP, (c) CA, (d) LSV, (e) PCE, (f) EIS.

Table 3
Open-circuit potential (OCP), photocurrent density, photo-conversion efficiency obtained from electrochemical analysis.

Sample	OCP value (V vs. Hg/HgO)	OCP_{light_on} (V vs. Hg/HgO)	OCP_{light_off} (V vs. Hg/HgO)	Photocurrent density (mA cm^{-2}) @ 1.23 V vs. Hg/HgO	Photo-conversion efficiency (%) @ 0.1V RHE
Pure TNTs	0.480	−0.647	−0.167	4.519	1.00
(1) rGO-TNTs	0.547	−0.712	−0.166	6.846	1.46
Ho-TNTs	0.502	−0.688	−0.187	5.821	1.16
(0.25) rGO-Ho-TNTs	0.522	−0.698	−0.176	6.394	1.31
(0.5) rGO-Ho-TNTs	0.557	−0.732	−0.175	7.153	1.47
(1) rGO-Ho-TNTs	0.577	−0.727	−0.149	7.476	1.53
(2) rGO-Ho-TNTs	0.565	−0.737	−0.172	7.165	1.48
(4) rGO-Ho-TNTs	0.536	−0.682	−0.146	6.472	1.32

attributed to suppressed recombination of photogenerated e^-/h^+ pairs, as rGO stabilizes the interfacial electronic structure and promotes charge separation [26].

The E_V values for all samples were determined from the difference between the E_F and E_L obtained from the UPS spectra (Fig. 6(a and b)), relative to E_{Vac}. Here, E_F is represented as the negative value of Φ [64]. As summarized in Table 2, the E_V values of pure TNTs, (1)rGO–TNTs, Ho–TNTs, and (0.25, 0.5, 1, 2, 4)rGO–Ho–TNTs are −6.66, −6.03, −6.50, −6.22, −5.97, −5.68, −5.87, and −6.15 eV (vs. vacuum level = 0 eV), respectively. Among them, (1)rGO-Ho-TNTs exhibits the highest E_V (−5.68 eV). Subsequently, all calculated energy parameters (E_L, E_F, Φ, E_V, and E_C) were converted to the reversible hydrogen electrode (RHE) scale using Equation (3) [64].

$$E(\text{V vs. RHE}) = E(E_L, E_F, \Phi, E_V, E_C) - 4.5\ \text{V} + 0.0591 \times \text{pH} \quad (3)$$

Here, E refers to the measured energy value (E_L, E_F, Φ, E_V, or E_C). The reference energy levels of −4.44 eV vs. vacuum (H^+/H_2) and −5.67 eV vs. vacuum (O_2/H_2O) were also converted to the RHE scale to compare the potentials of the hydrogen and oxygen evolution reactions [8].

The E_g is an intrinsic property determined by the atomic arrangement of a semiconductor, and the potentials of the E_V and E_C correspond to fixed energy levels. Fig. 7(a) shows the energy-band diagrams of the samples, expressed in two potential units (V vs. RHE and V vs. vacuum level), constructed using the E_g, E_L, E_F, Φ, E_V, and E_C values obtained from the Tauc plots of UV-DRS and UPS data. A comparison of pure TNTs and heterojunctions (with Ho and rGO) shows that the modification of the TNTs facilitates the migration and separation of photogenerated charge carriers and shifts E_V in the negative direction, resulting in a narrower E_g Refs. [9,64,65]. In particular, when rGO, a nonmetallic material with high electrical conductivity, and Ho, a metallic dopant with a broad light absorption range, are incorporated into TNTs to form the rGO–Ho–TNT ternary architecture, the system effectively accepts and transfers electrons generated by TiO_2 or Ho under UV–visible light irradiation. This efficient electron-transfer process enhances photocurrent generation by suppressing e^-/h^+ recombination [44,65], thereby expanding the light absorption range of TiO_2 and shifting the absorption edge toward the visible region. Consequently, the photoexcited electrons at the electrode interface are transferred from the E_C of the TNTs to Ho or rGO, where they react with H_2O or H^+ ions to produce H_2 [23].

3.2. Photoelectrochemical properties

Fig. 7(b–f) shows the OCP, CA, LSV, PCE, EIS results for pure TNTs, (1)rGO–TNTs, Ho–TNTs, and (0.25, 0.5, 1, 2, 4)rGO–Ho–TNTs. Fig. 7(b) shows the OCP results, which indicate the potential difference between the photoanode and cathode in the absence of an external bias. The measurements were performed under alternating light/dark conditions at 60 s intervals. Under dark conditions, the E_F is farthest from the conduction band minimum (E_{CB}), resulting in a low OCP_{dark}. Under light conditions, the quasi-Fermi level (E_{qF}) shifts closer to the E_{CB}, yielding a higher OCP_{light} [8,66]. As shown in Table 3, the (1)rGO–Ho–TNT electrode exhibits the highest OCP of 0.577 V (vs. Hg/HgO). This suggests that rGO drop-casting significantly enhances the separation efficiency of photogenerated e^-/h^+ pairs within the photoanode [26]. In general, a higher OCP corresponds to a higher photovoltage, carrier concentration, and carrier mobility of the photoanode, and suppressed e^-/h^+ recombination, thereby enhancing the photocurrent density [66,67].

The CA analysis results (Fig. 7(c)) show the photocurrent density and energy conversion efficiency as functions of charge transfer suppression and e^-/h^+ recombination rates at the electrode–electrolyte interface [65]. Under light/dark cycles at 60 s intervals under an applied potential of 1.5 V (vs. Hg/HgO), the photocurrent rapidly increases under illumination and then quickly decays in the dark, reaching a stable equilibrium state. Among the samples, (1)rGO–Ho–TNTs exhibits the highest photocurrent density, which is approximately 1.7 and 1.3 times higher than those of pure TNTs and Ho–TNTs, respectively. This enhancement is attributed to the superior electron-accepting capability and high electrical conductivity of rGO, which effectively suppresses charge recombination [65].

Fig. 7(d) illustrates the photocurrent density–voltage (J–V) characteristics measured over the potential range of −1.0 to 2.0 V (vs. Hg/HgO). Pure TNTs generate the smallest J, which steadily increases with Ho doping and rGO drop-casting. Among all samples, the (1)rGO–Ho–TNT electrode exhibits the highest J, even at low voltages, reaching 7.476 mA cm^{-2} at 1.23 V (vs. Hg/HgO). The improved separation and transport of photoexcited e^-/h^+ pairs significantly enhances J [68].

Fig. 7(e) presents the PCE, which quantifies the conversion of incident light into electrical energy and serves as a key performance metric for PEC electrodes. The PCE was calculated from the LSV results (Table 3 and Fig. 7(d)) using the following equation [69]:

$$\eta = \frac{I \times (1.23 - V_{bias})}{P_{light}} \times 100\% \quad (4)$$

where η, I, V_{bias}, and P_{light} denote the PCE (%), measured photocurrent density (A cm^{-2}), applied potential (V vs. RHE), and incident light intensity (W cm^{-2}), respectively. The PCE values of the samples were 1.00%, 1.46%, 1.16%, 1.31%, 1.47%, 1.53%, 1.48%, and 1.32%. (Table 3) Notably, the PCE of (1) rGO–Ho–TNTs was 1.53, 1.32, and 1.05 times higher than those of pure TNTs, Ho–TNTs, and (1)rGO–TNTs, respectively.

Fig. 7(f) shows the Nyquist plots obtained from EIS measurements, which were fitted using the inset equivalent circuit model. The EIS measurements were performed at a bias potential of −0.5 V over a frequency range of 10^5–10^{-2} Hz. Here, R_s (solution resistance) is the ohmic resistance of the electrolyte–substrate interface, and R_{ct} (charge-transfer resistance) is the charge-transfer resistance associated with oxidation at

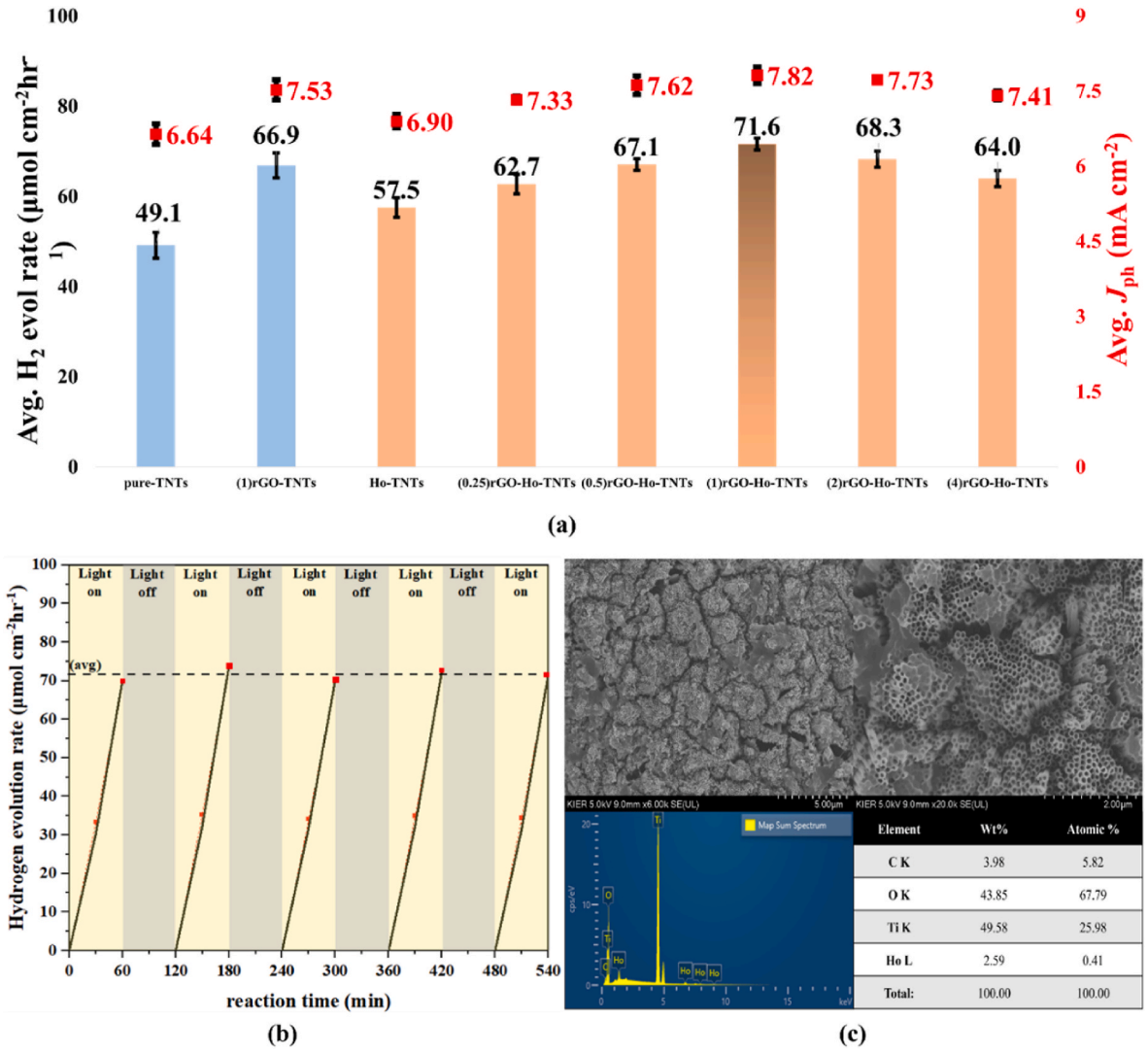


Fig. 8. (a) Hydrogen evolution rate and average current density of the as-prepared samples. (b) Durability of (1)rGO-Ho-TNTs over five consecutive cycles, (c) SEM and EDS analysis of (1)rGO-Ho-TNTs after durability test.

the photoanode/electrolyte interface. The R_{ct} values decrease in the following order: pure TNTs > Ho–TNTs > (0.25)rGO–Ho–TNTs > (4)rGO–Ho–TNTs > (1)rGO–TNTs > (0.5)rGO–Ho–TNTs > (2)rGO–Ho–TNTs > (1)rGO–Ho–TNTs. Overall, a concurrent decrease in R_{ct} and increase in constant phase element (*CPE*; interfacial capacitance) are observed. This trend is attributable to impurity energy levels introduced by Ho doping and rGO drop-casting, which create additional electronic states and hopping sites, thereby promoting charge transfer across the electrode–electrolyte interface. Accordingly, the improved PEC performance can be attributed to accelerated interfacial charge separation and transport enabled by the impurity energy levels [65,70,71].

Overall, the PEC results (Fig. 7(b–f)) and supporting analyses demonstrate a consistent performance trend, identifying 1 μg cm^{-2} as the optimum rGO loading for achieving maximum PEC performance.

3.3. Photoelectrochemical performance of rGO–Ho–TNTs

The energy diagram in Fig. 7(a) shows that all samples possess H^+/H_2 and O_2/H_2O potentials located within their E_g, indicating that they are suitable for PEC water splitting. Fig. 8(a) presents the average hydrogen evolution rate and average *J* for each sample, confirming the synergistic effects associated with variations in Ho doping and rGO content. The overall performance enhancement follows the trend: pure TNTs < Ho–TNTs < (0.25)rGO–Ho–TNTs < (4)rGO–Ho–TNTs < (1)rGO–TNTs < (0.5)rGO–Ho–TNTs < (2)rGO–Ho–TNTs < (1)rGO–Ho–TNTs.

Among all samples, the (1)rGO–Ho–TNT electrode exhibits the best performance. The hydrogen evolution rate and *J* are approximately 1.5 and 1.2 times higher than those of pure TNTs and approximately 1.3 and 1.1 times higher than those of Ho–TNTs, respectively. The enhanced hydrogen evolution rate and *J* are attributed to the expansion of the light-absorption wavelength range and higher photoreaction rate, resulting from the lower Φ and narrower E_g. Additionally, Fig. 8(b) presents the stability evaluation results for the (1)rGO–Ho–TNT electrode. The hydrogen evolution test was performed for 1 h under illumination, followed by Ar purging for 1 h in the dark, and this cycle was repeated five times. As a result, it was confirmed that the hydrogen generation activity remains stable during repeated cycles. Fig. 8(c) shows the electrode surface after the durability test. SEM images confirmed the preservation of the nanotube structure and the rGO coating, with no observable evidence of structural damage or collapse. EDS analysis revealed no significant changes in the major elemental composition compared with the initial electrode, confirming compositional stability. These results confirm that the electrode maintained structural and chemical stability under repeated PEC test.

4. Conclusion

Binary and ternary composite electrodes (Ho–TNTs and rGO–Ho–TNTs) were successfully fabricated via anodization, electrochemical doping using Ho aqueous solutions, and drop-casting of controlled rGO concentrations. The rGO loading on the electrode surface was identified as a key parameter significantly affecting the electrode performance. Based on band-structure using XPS, UPS, and UV-DRS (Tauc plots), (1)rGO–Ho–TNTs exhibited the smallest crystallite size (261 Å), the lowest work function (3.25 eV), and the narrowest bandgap (2.79 eV) among the prepared electrodes. These structural and electronic features of the composite material facilitate broader light absorption and efficient suppression of e^-/h^+ recombination, thereby increasing the photocurrent and photocatalytic activity. In electrochemical analysis, (1)rGO–Ho–TNTs exhibited 20.2% improved open open-circuit potential circuit potential and 65.4% increased photocurrent density compared to pure TNTs. In PEC water splitting experiments, the hydrogen evolution rate improved by 45.8% compared to pure TNTs and 24.5% compared to Ho–TNTs. In addition, the PCE of (1) rGO–Ho–TNTs was 1.5, 1.1, and 1.4 times that of pure TNTs, Ho–TNTs, and (1)rGO–TNTs, respectively. This study demonstrated that photocatalytic performance can be improved by introducing impurity energy levels utilizing holmium ions and optimizing the rGO drop-cast concentration. These results are expected to stimulate further research on photoanodes decorated with various elements and rGO for sustainable hydrogen production, including PEC water splitting and solar-driven H_2 generation.

CRediT authorship contribution statement

Hyeonmin Jung: Writing – original draft, Visualization, Validation, Project administration, Methodology, Formal analysis, Data curation, Conceptualization. **Minseo Kim:** Methodology, Investigation, Conceptualization. **Hyekyung Cho:** Methodology, Formal analysis, Conceptualization. **Hyunku Joo:** Project administration, Methodology, Investigation, Conceptualization. **Kyoung-Soo Kang:** Resources, Project administration, Funding acquisition. **Hyunjoon Lee:** Validation, Software, Investigation. **Hansung Kim:** Software, Investigation, Formal analysis. **Yeomin Yoon:** Software, Investigation, Formal analysis. **Jaekyung Yoon:** Writing – review & editing, Validation, Supervision, Project administration, Methodology, Data curation, Conceptualization. **Kwangbok Yi:** Validation, Supervision, Investigation, Formal analysis.

Declaration of competing interest

The authors declare that they have no known competing financial interests or personal relationships that could have appeared to influence the work reported in this paper.

Acknowledgments

Funding: This study was supported by the Project of Technology Independence for Green Hydrogen through the National Research Foundation of Korea (NRF), funded by the Ministry of Science and ICT (RS-2024-00466616).

Glossary

Ho	Holmium
GO	Graphene oxide
rGO	Reduced graphene oxide
TNTs	TiO_2 nanotubes
(x)	The amount of rGO (μg cm^{-2})
e^-/h^+	Electron/hole
E_V	Valance band
E_C	Conduction band
E_L	Low binding energy
E_F	Fermi level
Φ	Work function
E_{Vac}	Vacuum level
E_{CB}	Conduction band minimum
E_{qF}	Quasi-Fermi level
$E_{cu\text{-}off}$	Secondary cut-off energy
$h\nu$	Photon (excitation) energy
J	Photocurrent density (mA cm^{-2})
R_s	Solution resistance (Ω)
R_{ct}	Charge-transfer resistance (Ω)
CPE	Constant phase element (interfacial capacitance)
Z'	Real part of impedance (Ω)
$-Z''$	Negative imaginary part of impedance (Ω)
n	CPE exponent (dimensionless)
Q	CPE constant (units vary with n)

Data availability

Data will be made available on request.

References

[1] A.R. Marlinda, N. Yusoff, S. Sagadevan, M.R. Johan, Recent developments in reduced graphene oxide nanocomposites for photoelectrochemical water-splitting applications, Int. J. Hydrogen Energy 45 (2020) 11976–11994, https://doi.org/10.1016/j.ijhydene.2020.02.096.

[2] H. Cho, H. Joo, H. Kim, J.E. Kim, K.S. Kang, J. Yoon, Improved photoelectrochemical properties of TiO_2 nanotubes doped with Er and effects on hydrogen production from water splitting, Chemosphere 267 (2021) 129289, https://doi.org/10.1016/j.chemosphere.2020.129289.

[3] M. Wang, J. Ioccozia, L. Sun, C. Lin, Z. Lin, Inorganic-modified semiconductor TiO_2 nanotube arrays for photocatalysis, Energy Environ. Sci. 7 (2014) 2182–2202, https://doi.org/10.1039/c4ee00147h.

[4] J. He, A. Kumar, M. Khan, I.M.C. Lo, Critical review of photocatalytic disinfection of bacteria: from noble metals- and carbon nanomaterials-TiO_2 composites to challenges of water characteristics and strategic solutions, Sci. Total Environ. 758 (2021) 143953, https://doi.org/10.1016/j.scitotenv.2020.143953.

[5] N Al Abass, T.F. Qahtan, A.M. Alansi, A. Bubshait, Y.A. Alwadei, Basiry N. Al, et al., Black TiO_2 nanotube arrays: bifunctional electrocatalytic performance for alkaline water splitting, Fuel 388 (2025) 134300, https://doi.org/10.1016/j.fuel.2025.134300.

[6] Y. Son, R. Jung, J.E. Yoo, K. Lee, Interfacial charge transfer modulation via phase junctions and defect control in spaced TiO_2 nanotubes for enhanced photoelectrochemical water splitting, Sol. RRL 9 (2025) 1–8, https://doi.org/10.1002/solr.202500334.

[7] M. Kim, H. Jung, H. Cho, H. Joo, K.S. Kang, H. Kim, et al., Enhanced catalytic activity and hydrogen production of Ho-TiO_2 nanotubes prepared under various pH conditions, Appl. Surf. Sci. 689 (2025) 162484, https://doi.org/10.1016/j.apsusc.2025.162484.

[8] H. Cho, H. Joo, H. Kim, J.E. Kim, K.S. Kang, H. Jung, et al., Enhanced photoelectrochemical activity of TiO_2 nanotubes decorated with lanthanide ions for hydrogen production, Catalysts 12 (2022) 1–14, https://doi.org/10.3390/catal12080866.

[9] H. Cho, H. Joo, H. Kim, J.E. Kim, K.S. Kang, J. Yoon, Enhanced photocatalytic activity of TiO_2 nanotubes decorated with erbium and reduced graphene oxide, Appl. Surf. Sci. 565 (2021) 150459, https://doi.org/10.1016/J.APSUSC.2021.150459.

[10] M. Tayebi, M. Kolaei, A. Tayyebi, Z. Masoumi, Z. Belbasi, B.K. Lee, Reduced graphene oxide (RGO) on TiO_2 for an improved photoelectrochemical (PEC) and photocatalytic activity, Sol. Energy 190 (2019) 185–194, https://doi.org/10.1016/j.solener.2019.08.020.

[11] K. Singh, S. Harish, A.P. Kristy, V. Shivani, J. Archana, M. Navaneethan, et al., Erbium doped TiO_2 interconnected mesoporous spheres as an efficient visible light catalyst for photocatalytic applications, Appl. Surf. Sci. 449 (2018) 755–763, https://doi.org/10.1016/j.apsusc.2018.01.279.

[12] V.R. Chappidi, K.V. Seshaiah, S. Madduri, S.S.K. Raavi, Rare-earth-doped TiO_2 photoanode DSSCs for indoor photovoltaics: a comparative study, J. Mater. Sci. Mater. Electron. 35 (2024) 1–13, https://doi.org/10.1007/s10854-024-12261-9.

[13] S. Rani, S. Singh, B. Pal, Core-shell structure of reduced graphene oxide@Ag–TiO_2 for photocatalytic H_2O splitting and CH_3OH dehydrogenation under UV light irradiation, Int. J. Hydrogen Energy 49 (2024) 910–924, https://doi.org/10.1016/j.ijhydene.2023.09.214.

[14] D. Boikanyo, S.B. Mishra, S. Ray, S.D. Mhlanga, A.K. Mishra, Structure-activity relationships of Er^{3+} and MWCNT-modified TiO_2: enhancing the textural and optoelectronic properties of TiO2, J. Phys. Chem. C 123 (2019) 31246–31261, https://doi.org/10.1021/acs.jpcc.9b08420.

[15] S. Girish Kumar, R. Kavitha, Lanthanide ions doped ZnO based photocatalysts, Sep. Purif. Technol. 274 (2021) 118853, https://doi.org/10.1016/j.seppur.2021.118853.

[16] J. Li, X. Tian, W. Bao, J. Zhao, Z. Jiang, Recent advances in the development and applications of lanthanide-based luminescent materials: a comprehensive review, Discov. Appl. Sci. 7 (2025), https://doi.org/10.1007/s42452-025-07862-w.

[17] P. Mazierski, W. Lisowski, T. Grzyb, M.J. Winiarski, T. Klimczuk, A. Mikołajczyk, et al., Enhanced photocatalytic properties of lanthanide-TiO_2 nanotubes: an experimental and theoretical study, Appl. Catal. B Environ. 205 (2017) 376–385, https://doi.org/10.1016/j.apcatb.2016.12.044.

[18] P. Xiang, C. Tang, K. Ma, X. Li, Highly efficient and robust oxygen vacancy-rich molybdenum trioxide aerogel evaporator for photothermal conversion and clean water generation, Desalination 594 (2025) 118281, https://doi.org/10.1016/j.desal.2024.118281.

[19] X. Jiang, C. Tang, X. Li, Z. Chen, Atomically precise Ni nanoclusters supported on CNT confined in hydrogel for efficient solar water evaporation: understanding synergistic effect of Ni nanoclusters and CNT on photothermal conversion, Chem. Eng. J. 521 (2025) 166473, https://doi.org/10.1016/j.cej.2025.166473.

[20] H. Shu, C. Tang, X. Li, Z. Chen, CuBTC-derivatives engineered into aerogel for water remediation: Solar-thermal desalination and pollutant degradation via peroxymonosulfate activation, Colloids Surfaces A Physicochem Eng Asp 735 (2026) 139505, https://doi.org/10.1016/j.colsurfa.2026.139505.

[21] H. Shu, X. Li, C. Tang, Z. Chen, Nickel clusters synergized with 1T-MoS_2 for enhanced photothermal conversion enabling efficient seawater desalination and wastewater purification, Sol. Energy Mater. Sol. Cells 299 (2026) 114225, https://doi.org/10.1016/j.solmat.2026.114225.

[22] R. Tarcan, O. Todor-Boer, I. Petrovai, C. Leordean, S. Astilean, I. Botiz, Reduced graphene oxide today, J. Mater. Chem. C 8 (2020) 1198–1224, https://doi.org/10.1039/c9tc04916a.

[23] L. Kuang, W. Zhang, Enhanced hydrogen production by carbon-doped TiO_2 decorated with reduced graphene oxide (rGO) under visible light irradiation, RSC Adv. 6 (2016) 2479–2488, https://doi.org/10.1039/c5ra26096e.

[24] F. Nazer, Z. Khakpour, A. Maghsoudipour, S. Hajati, Synthesis and characterization of black hydrogenated TiO_2-rGO nanocomposites with enhanced photocatalytic activity, Int. J. Hydrogen Energy 78 (2024) 148–156, https://doi.org/10.1016/j.ijhydene.2024.06.260.

[25] J. Ma, J. Dai, Y. Duan, J. Zhang, L. Qiang, J. Xue, Fabrication of PANI-TiO_2/rGO hybrid composites for enhanced photocatalysis of pollutant removal and hydrogen production, Renew. Energy 156 (2020) 1008–1018, https://doi.org/10.1016/j.renene.2020.04.104.

[26] Z. Wang, Y. Li, C. Zhang, J. Wu, K. Cui, Q. Li, Degradation of AO7 through RGO/TiO_2 nanotube arrays photoanode in UV/electrical coupling system:performance and mechanism analysis, Opt. Mater. 149 (2024) 115030, https://doi.org/10.1016/j.optmat.2024.115030.

[27] T. Thanh, D. Nguyen, D. Nguyen, N. Nhu, T. Pham, Applied surface science surface modification of TiO_2 photoanode in dye-sensitized solar cells using reduced graphene oxide : a computational and experimental study, Appl. Surf. Sci. 683 (2025) 161783, https://doi.org/10.1016/j.apsusc.2024.161783.

[28] R. Hou, J. Ying, F. Wang, X. Lv, D. Huang, The effect of oxygen functional groups on TiO_2/RGO composites for the degradation of unsymmetrical dimethylhydrazine, J. Mater. Res. Technol. 20 (2022) 2809–2818, https://doi.org/10.1016/j.jmrt.2022.08.030.

[29] M.B. Askari, P. Salarizadeh, State-of-the-art review on reduced graphene oxide for supercapacitor electrode applications, Results Eng. 28 (2025) 107429, https://doi.org/10.1016/j.rineng.2025.107429.

[30] T.C.S. Girisun, T. Sharmila, Synergistic impact of Au/rGO decoration on vertically aligned TiO_2 nanorod arrays for advanced plasmonic dye-sensitized solar cells, Mater. Sci. Semicond. Process. 196 (2025) 109680, https://doi.org/10.1016/j.mssp.2025.109680.

[31] T. Kavitha, O. Rojviroon, R. Rajendran, T. Rojviroon, Construction of hybrid 2D g-C_3N_4/$BiVO_4$ photocatalyst decorated with RGO for enhancing the H_2 production and photocatalytic degradation of antibiotics, J. Porous Mater. 32 (2025) 1457–1469, https://doi.org/10.1007/s10934-025-01778-x.

[32] C. Yan, Z. Tang, L. Wang, Z. Piao, H. Wang, Y. Zhang, Covalently linking reduced graphene oxide facilitated electrodeposition of MoS_2 on silicon pyramidal photocathode to enhance hydrogen evolution, Langmuir 40 (2024) 12427–12436, https://doi.org/10.1021/acs.langmuir.4c00679.

[33] L. Hu, X. Jiang, J. Wang, H. Wang, Y. Zhang, X. Yi, et al., Direct Utilization of a HF-Treated Si Photocathode for Efficient Hydrogen Production, Nano Lett. 25 (2025) 6051–6058, https://doi.org/10.1021/acs.nanolett.4c06302.

[34] S. Guo, X. Zhao, W. Zhang, W. Wang, Optimization of electrolyte to significantly improve photoelectrochemical water splitting performance of ZnO nanowire arrays, Mater. Sci. Eng. B 227 (2018) 129–135, https://doi.org/10.1016/j.mseb.2017.09.020.

[35] R. Ahmed, Y. Xu, G. Zangari, Water splitting vs. sulfite oxidation: an assessment of photoelectrochemical performance of TiO_2 nanotubes modified by CdS/CdSe nanoparticles, Electrochim. Acta 259 (2018) 1095–1103, https://doi.org/10.1016/j.electacta.2017.12.088.

[36] S. Chen, W. Zhou, Y. Ding, G.B. Zhao, J.H. Gao, Energy-saving cathodic hydrogen production enabled by anodic oxidation of aqueous sodium sulfite solutions, Energy Fuels 34 (2020) 9058–9063, https://doi.org/10.1021/acs.energyfuels.0c01589.

[37] M.A.M. Khan, P. Nain, S. Kumar, A.A. Ansari, M. Ahamed, M. Shahabuddin, Improved photocatalytic and electrochemical activities of (Nd^{3+}, Yb^{3+}) co-doped TiO_2 nanoparticles synthesized by hydrothermal protocol, J. Mater. Sci. Mater. Electron. 35 (2024) 1–16, https://doi.org/10.1007/s10854-024-13904-7.

[38] T. Cao, Y. Gao, W. Xia, X. Qi, Materials and Hydrogen Production via Visible Light, 2024.

[39] M. Yangui, K. Saidi, C. Hernández-Álvarez, M. Dammak, I.R. Martín, Ratiometric luminescent thermometry with excellent sensitivity in the visible and near-infrared (NIR-II/III) based on thermally coupled and non-thermally coupled energy levels of Er^{3+} and Ho^{3+} ions, J. Alloys Compd. 1010 (2025), https://doi.org/10.1016/j.jallcom.2024.177958.

[40] Z.H. Mahmoud, H.N.K. AL-Salman, H.H. Hussein, C.Y. Hsu, High-performance TiO_2/perovskite solar cell based GO as hole transport layer, J. Mater. Sci. Mater. Electron. 35 (2024) 1–15, https://doi.org/10.1007/s10854-024-12998-3.

[41] R. Yan, Q. Wu, G. Lin, L. Chen, X. Song, S. Luo, et al., Inhibition of Salmonella typhimurium and Listeria monocytogenes in coconut juice by graphene-doped photocatalyst rGO/TiO_2, Food Chem. 463 (2025) 141103, https://doi.org/10.1016/j.foodchem.2024.141103.

[42] R. Saha, Thukral A. Neha, A. Pal, P. Saini, Sunlight responsive superhydrophilic rGO-TiO_2 nanocomposite coatings for photovoltaic applications, Diam. Relat. Mater. 149 (2024) 111603, https://doi.org/10.1016/j.diamond.2024.111603.

[43] M. Ruidíaz-Martínez, M.A. Álvarez, M.V. López-Ramón, G. Cruz-Quesada, J. Rivera-Utrilla, M. Sánchez-Polo, Hydrothermal synthesis of RGO-TiO_2 composites as high-performance UV photocatalysts for ethylparaben degradation, Catalysts 10 (2020), https://doi.org/10.3390/catal10050520.

[44] B. Zhang, D. Li, W. Xiong, M. Wu, B. Chu, H. Liu, et al., Fabrication of three-dimensional hollow nanocassette photocatalysts RE-TiO_2 (RE = La, Ce, Sm, Yb, and Tm) with enhanced pesticide degradation activity and highly exposed (1 0 1) crystal planes, Appl. Surf. Sci. 626 (2023) 157239, https://doi.org/10.1016/j.apsusc.2023.157239.

[45] A.A. Khan, A.T. Partho, M.H. Arnab, M.A. Khyam, N. Kumar, M. Tahir, Recent advances in Lanthanum-based photocatalysts with engineering aspects for photocatalytic hydrogen production: a critical review, Mater. Sci. Semicond. Process. 184 (2024), https://doi.org/10.1016/j.mssp.2024.108809.

[46] I.V. Ayala, E. Mejía-Ospino, C. Gonzalez-Arias, R. Cabanzo-Hernández, E.D. V-Niño, Evaluation of sol-gel and solvothermal method on titanium dioxide and reduced graphene oxide nanocomposite, J. Phys., Conf. Ser. 2726 (2024), https://doi.org/10.1088/1742-6596/2726/1/012003.

[47] M. Chinnarani, S. Suresh, K.M. Prabu, M. Kandasamy, N. Pugazhenthiran, Facile synthesis of reduced graphene oxide and graphitic carbon nitride modified titanium dioxide nanospheres for photoanode of dye-sensitized solar cell, Inorg. Chim. Acta. 560 (2024) 121842, https://doi.org/10.1016/j.ica.2023.121842.

[48] S.N. Shkerin, A.N. Meshcherskikh, T.V. Yaroslavtseva, R.K. Abdurakhimova, Raman and photoluminescence spectra for Ho, Er, Tm, Yb, Lu, and Y doped Hafnia, Phys. Solid State 64 (2022) 1951, https://doi.org/10.21883/pss.2022.12.54392.435.

[49] B. Dziejarski, J. Serafin, D.F. Hernández-Barreto, J.C. Moreno-Piraján, L. Giraldo, N. Homs, et al., Chemical conversion of recovered carbon black (rCB) from end-of-life tires (ELTs) pyrolysis to reduced graphene oxide (rGO): from waste to advanced materials, J. Mater. Chem. C 13 (2024) 2753–2767, https://doi.org/10.1039/d4tc03556a.

[50] N. Xiong, Y. Guo, Y. Nie, Y. Yao, Z. Ying, W. Zhang, et al., An efficient photocatalytic material, rGO-TiO_2, that can be industrially produced: fabrication and structural characterization, Water (Switzerland) 17 (2025) 1–14, https://doi.org/10.3390/w17020161.

[51] T.T.D. Nguyen, D. Nguyen, N.N.T. Pham, P.T. Nguyen, Surface modification of TiO_2 photoanode in dye-sensitized solar cells using reduced graphene oxide: a computational and experimental study, Appl. Surf. Sci. 683 (2025) 161783, https://doi.org/10.1016/j.apsusc.2024.161783.

[52] M. Xing, F. Shen, B. Qiu, J. Zhang, Highly-dispersed Boron-doped graphene nanosheets loaded with TiO_2 nanoparticles for enhancing CO_2 photoreduction, Sci. Rep. 4 (2014) 1–7, https://doi.org/10.1038/srep06341.

[53] R. Larik, A. Balouch, E. Alveroğlu Durucu, H. Silah, Saqaf Jagirani M. Abdullah, et al., Electrochemical sensor for catechol detection: leveraging ITO@TiO_2/RGO/Pt nanocomposites for enhanced water quality monitoring, Mater. Sci. Eng. B 313 (2025), https://doi.org/10.1016/j.mseb.2024.117966.

[54] M. Abbas, M. Degani, S. Sheybani, T. Shah, M. Joy, K.J. Balkus, Synthesis and characterization of holmium based metal-organic frameworks, CrystEngComm (2024) 5567–5573, https://doi.org/10.1039/d4ce00592a.

[55] S. Alotibi, R.H. Al Otaibi, N.F. Al-Ablan, A.A. Al-Rashidi, M. Alyami, A. Kaiba, et al., Optimizing thermal reduction of graphene oxide for enhanced solar-driven water purification using rGO-TiO_2 nanocomposites, Phys. B Condens. Matter 699 (2025) 416821, https://doi.org/10.1016/j.physb.2024.416821.

[56] M.A.J. Felix, C. Ragumoorthy, T.W. Chen, S.M. Chen, G. Kiruthiga, A. Singh, et al., Fluid-specific detection of environmental pollutant moxifloxacin hydrochloride utilizing a rare-earth niobate decorated functionalized carbon nanofiber sensor platform, Environ. Res. 264 (2025) 120349, https://doi.org/10.1016/j.envres.2024.120349.

[57] J. Zhu, X.J. Shao, Z. Li, C.H. Lin, C.W.Q. Wang, K. Jiao, et al., Synthesis of holmium-oxide nanoparticles for near-infrared imaging and dye-photodegradation, Molecules 27 (2022) 1–12, https://doi.org/10.3390/molecules27113522.

[58] L. Peng, P. Nian, J. Feng, X. Han, B. Cui, S. Lu, et al., Photocatalytic degradation of aqueous rhodamine B by TiO_2/ZnO/rGO nanocomposite: photocatalytic activity and catalytic mechanism, Desalination Water Treat. 154 (2019) 268–282, https://doi.org/10.5004/dwt.2019.24040.

[59] S Bin Jeong, K.J. Heo, J.H. Yoo, D.G. Kang, L. Santoni, C.E. Knapp, et al., Photobiocidal activity of TiO_2/UHMWPE composite activated by reduced graphene oxide under white light, Nano Lett. 24 (2024) 9155–9162, https://doi.org/10.1021/acs.nanolett.4c00939.

[60] A. Mikolajczyk, E. Wyrzykowska, P. Mazierski, T. Grzyb, Z. Wei, E. Kowalska, et al., Visible-light photocatalytic activity of rare-earth-metal-doped TiO_2: experimental analysis and machine learning for virtual design, Appl. Catal. B Environ. 346 (2024) 123744, https://doi.org/10.1016/j.apcatb.2024.123744.

[61] M. Kumar, M. Pokhriyal, M. Gupta, G. Vijaya Prakash, S. Uma, R. Nagarajan, Optical property evaluation of thoria doped with heavier rare-earth oxides LnO1.5 (ln = Er^{3+}, Ho^{3+}, Tm^{3+}, and Yb^{3+}), J. Am. Ceram. Soc. 102 (2019) 1832–1842, https://doi.org/10.1111/jace.16053.

[62] P.H.M. Andrade, C. Volkringer, T. Loiseau, A. Tejeda, M. Hureau, A. Moissette, Band gap analysis in MOF materials: distinguishing direct and indirect transitions using UV–vis spectroscopy, Appl. Mater. Today 37 (2024) 102094, https://doi.org/10.1016/j.apmt.2024.102094.

[63] R. Xu, Y. Li, S. Feng, J. Wang, J. Zhang, X. Zhang, et al., Enhanced performance of planar perovskite solar cells using Ce-doped TiO_2 as electron transport layer, J. Mater. Sci. 55 (2020) 5681–5689, https://doi.org/10.1007/s10853-020-04409-9.

[64] R.T. Gao, J. Zhang, T. Nakajima, J. He, X. Liu, X. Zhang, et al., Single-atomic-site platinum steers photogenerated charge carrier lifetime of hematite nanoflakes for photoelectrochemical water splitting, Nat. Commun. 14 (2023), https://doi.org/10.1038/s41467-023-38343-6.

[65] E. Hajialilou, H. Asgharzadeh, S. Khameneh Asl, TiO_2/rGO/Cu_2O ternary hybrid for high-performance photoelectrochemical applications, Appl. Surf. Sci. 544 (2021), https://doi.org/10.1016/j.apsusc.2020.148832.

[66] K.H. Ye, H. Li, D. Huang, S. Xiao, W. Qiu, M. Li, et al., Enhancing photoelectrochemical water splitting by combining work function tuning and heterojunction engineering, Nat. Commun. 10 (2019) 1–9, https://doi.org/10.1038/s41467-019-11586-y.

[67] R. Guo, X. Zhang, Y. Chen, Y. Zhang, Internal electric field-induced high-efficiency piezo-photocatalytic performance in bimetal-regulated layered perovskite $SrBi_2Nb_2O_9$, Adv. Funct. Mater. (2024) 2408838, https://doi.org/10.1002/adfm.202408838, 1–16.

[68] F. Nasirpouri, L. Jafari-Foruzin, A. Farmani, H. Yadipour, N.S. Peighambardoust, Boosted photoelectrochemical activity of anodic titanium dioxide nanotubes by electrophoretically decorated nickel–aluminum layered double hydroxide, Mater. Res. Bull. 182 (2025) 113167, https://doi.org/10.1016/j.materresbull.2024.113167.

[69] J. Wang, L. Liccardo, H. Habibimarkani, E. Wierzbicka, T. Schultz, N. Koch, et al., Precise control of TiO_2 overlayer on hematite nanorod arrays by ALD for the photoelectrochemical water splitting, Sustain. Energy Fuels 8 (2024) 3753–3763, https://doi.org/10.1039/d3se01633a.

[70] W. Rehman, F. Saeed, S. Arain, M. Usman, B. Maryam, X. Liu, Enhanced photoelectrochemical water splitting using a $NiFe_2O_4$/NG@MIL-100(Fe)/TiO_2 composite photoanode: synthesis, characterization, and performance, J. Compos. Sci. 9 (2025) 1–20, https://doi.org/10.3390/jcs9050250.

[71] S. Cheng, Y. Cheng, T. Zhou, S. Li, D. Xie, X. Li, Enhanced photoelectrochemical performance of $BiVO_4$ photoanodes Co-Modified with borate and $NiFeO_x$, Micromachines 16 (2025) 1–15, https://doi.org/10.3390/mi16080866.